Dye Dispersion in the Seasonal Thermocline

DAVID P. VASHOLZ AND LARRY J. CRAWFORD

The Johns Hopkins University Applied Physics Laboratory, Laurel, MD 20707

(Manuscript received 14 May 1984, in final form 15 October 1984)

ABSTRACT

A dye dispersion experiment was performed in September, 1979, in the open ocean approximately 180 km off the east coast of Florida. An initially vertical sheet of dye extending from about 60 to 100 meters in depth and about 10 kilometers long was dispensed into the seasonal thermocline. Its subsequent evolution was recorded with an instrumented chain that included 25 fluorometers, which was towed back and forth across the dye sheet by another vessel. The dye sheet was crossed 17 times at ages varying from 6 minutes to slightly less than 4 hours. Two of the most apparent effects in the data were the importance of vertical shear and the presence of intermittency in the dye time series. It is found that the depth-averaged width of the dye sheet grows as time to the 3/2 power. There is good evidence that a shear–diffusion interaction is responsible for this growth, which implies an effective vertical diffusivity of (1.0 ± 0.5) cm^2 s^{-1}. Even though this is an upper-ocean experiment, there is some consistency with predictions based upon the observed "universality" of deep ocean random background internal waves. It is argued that the observed intermittency represents a level of detail that is not accessible from the usual partial-differential-equation approach employing an effective diffusivity.

1. Introduction

It is the purpose of this work to describe and present results of a field experiment to investigate the evolution of a vertical sheet of dye dispensed into the seasonal thermocline. The experiment was performed in September 1979, off the east coast of Florida.

There are three basic features of this experiment that together distinguish it from earlier efforts (for example, see Ewart and Bendiner, 1981; Kullenberg, 1977; and references cited therein). The first of these is the use of a towed chain of sensors that included 25 fluorometers and permitted a much greater sampling density than heretofore attained. The second is the overall geometry of the experiment, in which an initially vertical sheet of dye was produced, the evolution of which was then recorded. This particular initial condition, as will be seen, is especially conducive to the comparison of theory and experiment. The final distinguishing feature is the relatively short evolution times that were studied, ranging from six minutes to a little less than four hours.

The rest of this paper is organized into six sections. In Section 2 the basic experiment and test site are described. Section 3 is devoted to the analytic approach and a description of how the data were processed. In Section 4 various analysis results are presented. The width growth of the dye sheet turns out to be particularly amenable to quantitative analysis, which is presented in Section 5. In Section 6 an independent justification of a basic assumption is discussed. Section 7 is given over to a summary and general comments.

2. Experiment description

a. Dispensing and measurement systems

The dye dispensing system used to lay a vertical dye sheet in the ocean was towed by the R.V. *Cove*. It consisted of an above-water pumping subsystem, an in-water dye dispensing subsystem and the tow system depressor.

The pumping subsystem was located on the ship's deck. Fifty-five gallon, closed-head drums strapped to the deck contained the dye solution. A 20-foot, one-inch diameter rubber hose connected the barrels and the bronze gear dye pump, which was driven by a 2-horsepower motor. To minimize pressure fluctuations from the pump, an air cushion tank was fitted at the discharge of the pump. A digital display of the flow rate was available to the operator for monitoring and control purposes. The in-line pressure was measured between the filter and the dispensing system, and the output pressure was monitored at the pump discharge.

The in-water dye dispensing occurred over a 40–45 meter vertical section of the tow cable, resulting in the deposition of a thin dye-sheet in the ocean. Fastened to the armored cable (strength member) was a long section of feeder hose which was extended from the R.V. *Cove*'s deck to the depth desired for the upper limit of the dye sheet. The dye was dispensed from a section of ½-inch-ID hose approximately 53 meters long. This section contained 91 orifices spaced uniformly at a separation of 0.577 meter.

The towed vehicle used as a depressor for the dispensing system consisted of an I-beam fuselage

with "flap-plate" wings and stabilizers. It was fastened to the bottom of the strength member with a three-point towing bridle.

The dye system also included equipment designed to control the dispensing process, to monitor the system and to record data needed for subsequent analysis. The four key parameters that were recorded were dye pumping flow rates, depth of the depressor, ship's speed through the water and time of day.

For the fluorometry measurements discussed here, a dye mixture that contained 10% disodium fluorescein and 10% rhodamine WT was used. This particular mixture was selected in support of an effort to evaluate various water-soluble organic dyes for their suitability for ocean use and is not essential to the results reported herein. The dye mixture was dispensed into the ocean at a flow rate of 7.6 liters per minute while the R.V. *Cove* was traveling at a speed of 4.2 meters per second.

The primary measurement system consisted of a vertical array of 25 fluorometers, 40 thermistors, 5 conductivity cells and 6 depth transducers deployed from the M.V. *State Rebel* and towed through the water at 6 knots. The sensor platform consisted of a ½-inch armored tension towing cable surrounded by low-drag fairings which were free to rotate around the strength member. This configuration resulted in a chain catenary that was nearly vertical with the bottom-most sensor capable of reaching a depth of 160 meters with 183 meters of scope paid out and 90 meters horizontal offset at 6 knots. An important feature of the overboarding system was a mechanism inside the chain winch drum that allowed the wire pairs to be transferred continuously from the sensors to their electronics without using connectors or slip rings. This feature permitted the system to perform at very low noise levels. Depth maintenance was accomplished with a depressor attached to the bottom of the chain.

The 40 thermistors spanned a vertical distance of 56 meters with a vertical separation between adjacent sensors ranging from 1 to 2 meters. The thermistor locations bracketed those of the thermometers. The topside electronics included thermistor bridges whose design was based on the Sippican XBT circuit.

The 25 fluorometers spanned a vertical distance of about 45 meters with variable sensor spacings of 1, 2 and 3 meters. Ten fluorometers were made sensitive to rhodamine WT dye and the remaining fifteen were made sensitive to disodium fluorescein dye. A brief description of the fluorometers used in this experiment has been given by Keys and Hocheimer (1977). The only differences between the rhodamine and fluorescein fluorometers were in their optical filters and their amplifier gains, which were adjusted to give similar calibration curves. The sensitivity of these units is 3×10^{-11} gm cm^{-3} for rhodamine WT and fluorescein in clear ocean water and they have a time constant of about 0.15 seconds. During this experiment, the fluorometer outputs were sampled at 40 Hz. At a tow speed of 6 knots, these instruments were able to resolve horizontal scales as small as 0.5 meters.

Several measurement systems provided supporting environmental and ship's positional information during the experiment. A survey of the test area was conducted to determine the vertical distribution of temperature, salinity and density and their horizontal variability. While underway, a number of XBT probes were dropped to obtain temperature profiles. Additional environmental information was obtained from occasional CTD casts.

Each research vessel was equipped with two Loran-C receivers for determining continuous own-ship's position. Inspection of ship's tracks generated in real-time indicated point-to-point noise of about 25 meters. Periodic system accuracy checks were performed by comparing Loran-C derived positions with those obtained from satellite navigation.

b. Experimental procedures and data summary

The fluorometry data were obtained during an experiment performed on 11 September 1979. As shown in Fig. 1a, the test site was in the open ocean in the vicinity of 28°11′N, 78°24′W. A CTD cast of the upper 200 m of the ocean was made at 28°5.8′N, 78°2.09′W at a time corresponding to the end of the fluorometry measurements. The results are displayed in Fig. 2. More local measurements of the temperature profiles were obtained from the thermistors on the towed chain immediately prior to each dye trail crossing. These results are plotted in the scatter diagram of Fig. 3. As can be seen from these figures, the dye sheet was dispensed in a depth region where the buoyancy frequency was markedly nonuniform.

The overall geometry of the experiment is illustrated in Fig. 1b. It shows the tracks, in earth-fixed coordinates, of the R.V. *Cove* dispensing dye while maintaining an eastward course and the M.V. *State Rebel* making subsequent dye trail crossings. The initially thin vertical dye sheet was about 40 m high and 10 km long with its center at a depth of 80 m. All of the crossings were essentially normal to the trail. The segments of crossings during which dye was detected are also indicated in Fig. 1b. The lateral spacings between successive crossings were typically 300–500 m. The entire exercise was performed in rather calm seas, so that both dispensing and measurement systems experienced good depth stability. Data from the pressure transducers indicated rms depth fluctuation varying from 10 to 62 cm over the 17 crossings. Table 1 lists by crossing number the time that the chain of sensors crossed the center of detected dye for that crossing. Also included are the age of the dye trail and the rms depth fluctuation of the sensor

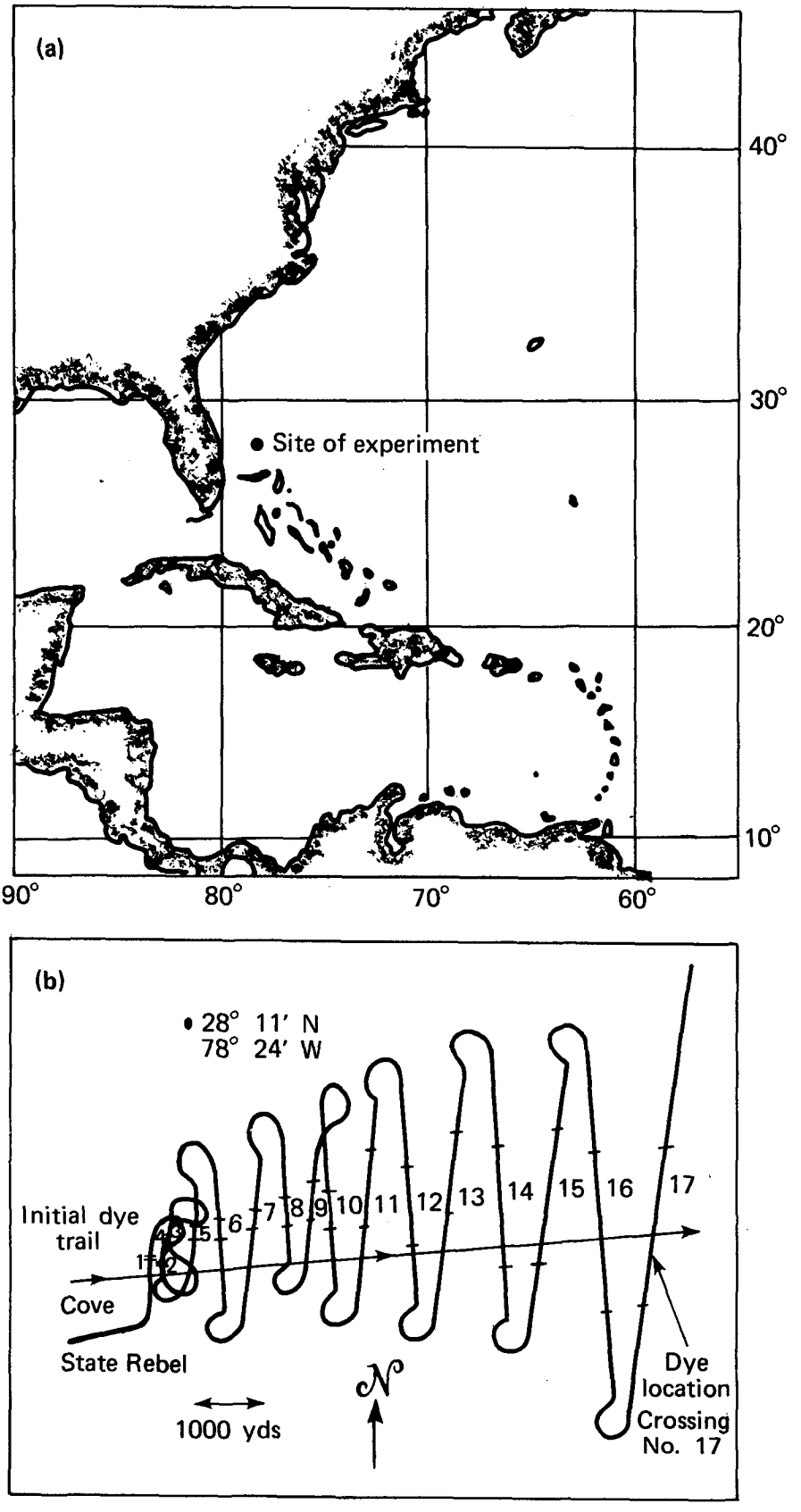

FIG. 1. (a) Map showing location of dye release experiment at 28°11′N, 78°24′W on 11 September 1979 and (b) detailed experiment geometry showing paths of R.V. *Cove* dispensing dye (1725 to 1805 GMT) and of M.V. *State Rebel* (1730 to 2200 GMT) making subsequent dye trail crossings.

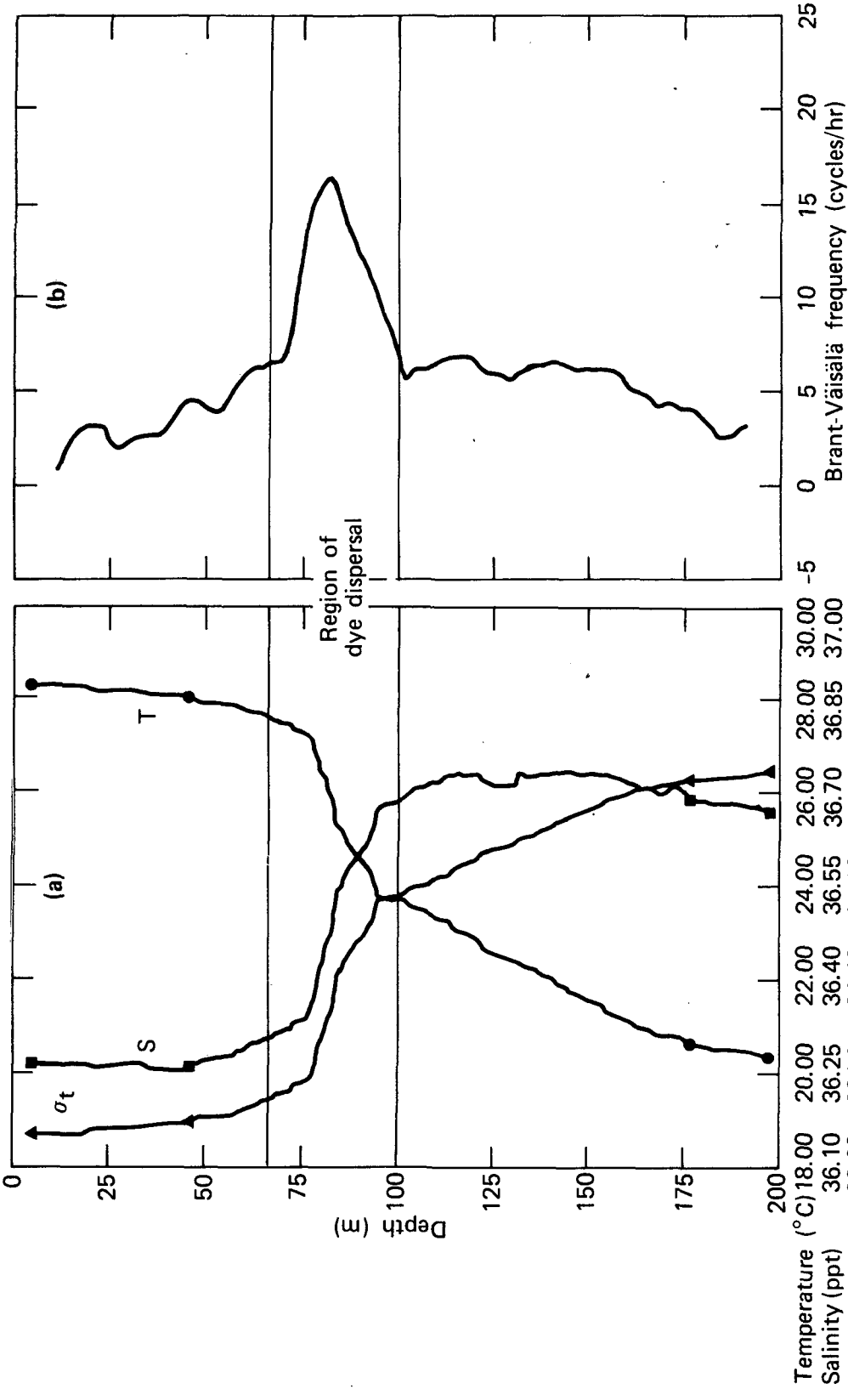

FIG. 2. Vertical profiles of (a) temperature, salinity and density and (b) Brunt-Väisälä frequency taken at 28°5.80'N and 78°2.09'W.

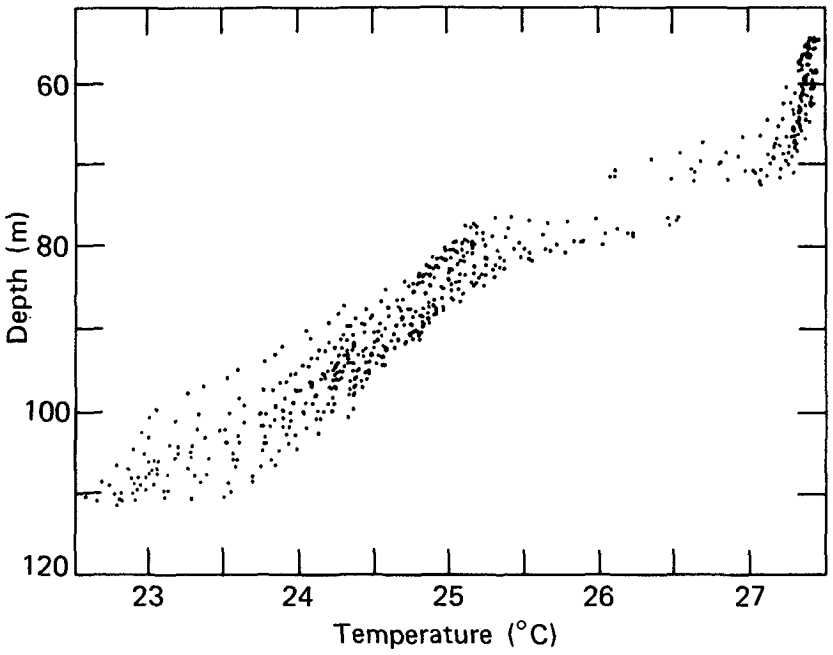

FIG. 3. Scatter plot of averaged thermistor chain data for the 17 dye sheet crossings.

chain for each crossing. Here dye trail age is defined as the elapsed time between center of dye detection and closest approach of the dye dispensing system to the point of detection. The experiment thus covered temporal scales to slightly less than four hours and spatial scales up to about 10 kilometers. The basic dataset consists of fluorometer time series for 25 fluorometers from 17 dye sheet crossings. Examples from two crossings are shown in Section 3.

TABLE 1. Dye crossing times, dye trail ages and sensor chain depth fluctuations.

Crossing	Time of crossing dye center (h:min:s GMT)	Age of dye trail* (h:min)	Depth fluctuations (cm)
1	17:34:47	00:06	17
2	17:42:48	00:14	41
3	17:50:50	00:21	37
4	18:00:37	00:31	62
5	18:10:34	00:40	10
6	18:22:36	00:49	18
7	18:38:43	01:04	20
8	18:52:31	01:15	36
9	19:05:15	01:26	32
10	19:19:57	01:40	34
11	19:36:32	01:53	17
12	19:54:18	02:09	32
13	20:13:09	02:25	27
14	20:34:44	02:43	36
15	20:54:31	03:00	34
16	21:18:52	03:21	31
17	21:45:24	03:45	45

* Dye dispensing occurred from 1725 to 1805 GMT.

3. Analytic approach

a. Basic considerations

We start with the fundamental advection–diffusion equation obeyed by the dye concentration field $c(\mathbf{x}, t)$. For present purposes it is given by

$$\frac{\partial c}{\partial t} + \mathbf{u} \cdot \nabla c - \mu \nabla^2 c = s(\mathbf{x}, t) \tag{1}$$

where μ is the molecular diffusion coefficient and $\mathbf{u}(\mathbf{x}, t)$ is the complete Eulerian velocity field. Here the source term $s(\mathbf{x}, t)$ is the rate (in units of mass per unit time per unit volume) at which the dye is being dispensed at position $\mathbf{x}$ and time t.

It is, of course, not possible to solve (1) directly for the problem at hand. Nonetheless, it is worth noting that the dye concentration field appears only linearly. This strongly suggests that the chances of confronting theory with experiment are maximized if the analysis is performed, wherever possible, in terms of quantities which are themselves linear in the concentration field.

b. Qualitative inputs

Our analysis approach is also motivated by various qualitative properties of the data which can readily be seen in the raw voltage time series. Examples of fluorometer time series from two of the crossings are shown in Figs. 4 and 5. Two of the fluorometers were inoperative during the experiment, so that 23 channels appear in these figures.

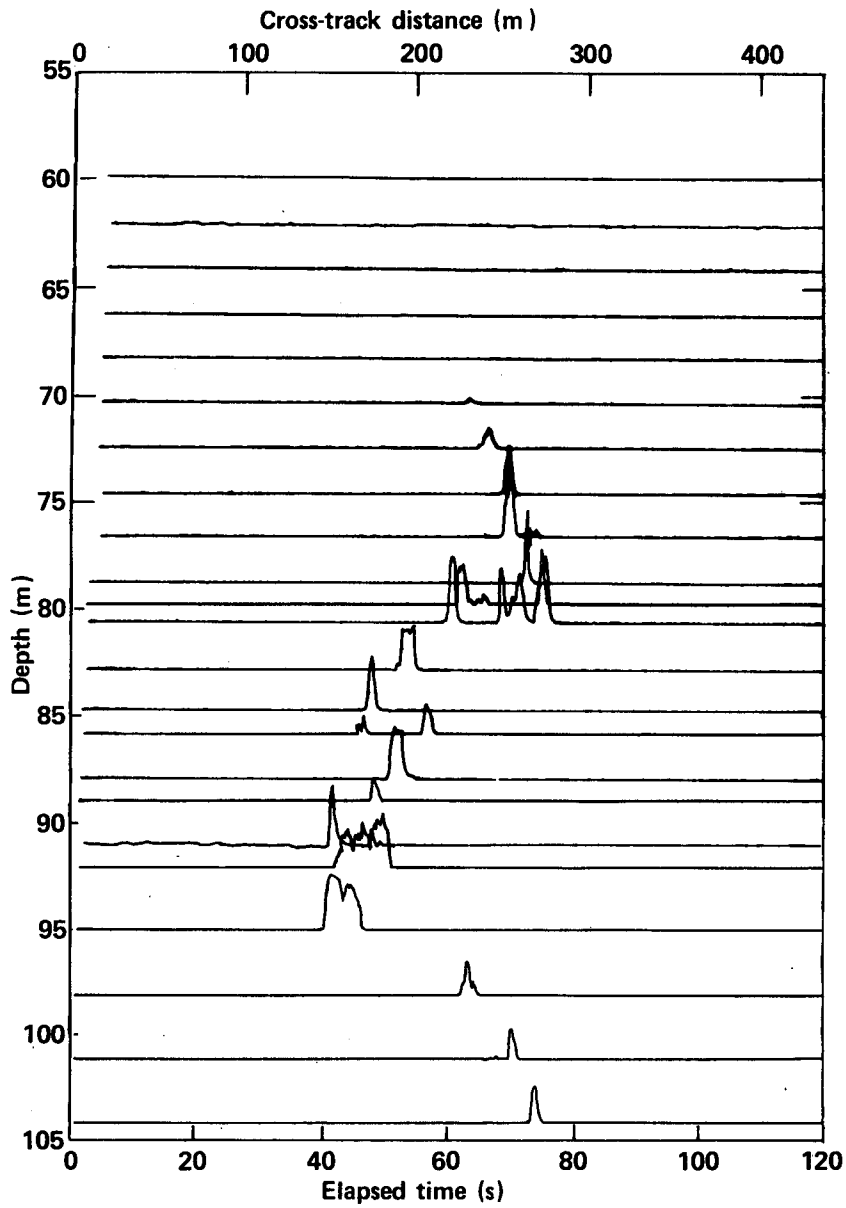

FIG. 4. Fluorometer time series for the third dye sheet crossing. The dye detected here has been in the water approximately 21 minutes. The fluorometer outputs have been arranged to reflect the geometry of the dye distribution.

These figures indicate that there has been a great deal of relative horizontal motion during the evolution of the dye sheet. Furthermore, there is no indication of any significant vertical transport relative to the depth range swept out by the fluorometers. This dominance of horizontal motions is not surprising, in view of the substantial stratification that was present.

A second qualitative feature readily apparent from Figs. 4 and 5 is that there is a marked degree of intermittency in the dye data. In particular, these figures indicate that intermittency is increasing with time, a property that is also borne out by the other crossings.

Owing to these basic qualitative features in the data, high priorities are given in the analysis to quantitative descriptions of the horizontal motions and the intermittency.

c. Dye moments

It would appear that the simplest way to describe horizontal motions while at the same time using quantities linear in the concentration field is to

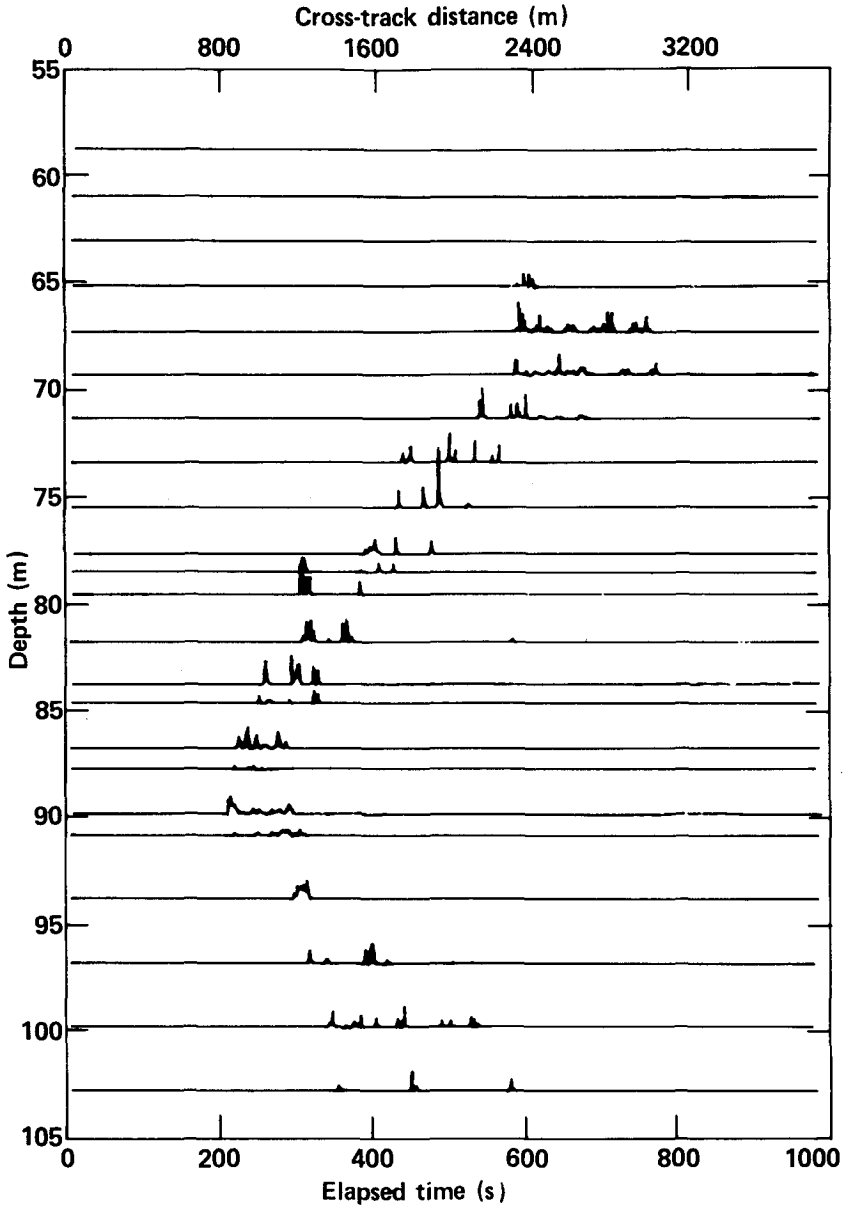

FIG. 5. The same as Fig. 4 but for the fifteenth crossing. The dye detected here has been in the water approximately 180 minutes. This crossing is aligned so that the fluorometer chain was towed in the same direction as it was for Fig. 4.

calculate moments for each of the dye time series and for each of the crossings. Let $c_{ij}(x)$ be the dye concentration as a function of distance traveled by fluorometer i during crossing j. Then the kth moment m_{ijk} is defined by

$$m_{ijk} = \int dx x^k c_{ij}(x). \tag{2}$$

For present purposes, only the three lowest moments are calculated for each combination of i and j. Together these three quantities specify, for each time series, the amount of dye present, its center of mass location and its width. Specifically, if $\bar{x}_{ij}$ and W_{ij} denote respectively the center of mass location and width corresponding to a particular time series, one has

$$\bar{x}_{ij} = \frac{m_{ij1}}{m_{ij0}}, \tag{3}$$

$$W_{ij}^2 = \frac{m_{ij2}}{m_{ij0}} - (\bar{x}_{ij})^2. \tag{4}$$

In effect, then, we are decomposing the dye-sheet

cross section for each of the crossings into a centerline determined by the $\bar{x}_{ij}$ and a symmetrized cross-section determined by the W_{ij}, as shown in Fig. 6.

To calculate the moments, the fluorometer calibrations were used to convert the voltage time series for each combination of i and j into a concentration time series having units of gm cm^{-3}. Taking into account the known speed at which the fluorometers were towed during each crossing, it was straightforward to compute discretized sums corresponding to the integral in (2).

d. Intermittency

Moments are of no apparent use in the description of the observed intermittency. More generally, it seems very unlikely that quantities linear in the concentration could be of use in such a description. The intermittency analysis is therefore based upon quantities directly suggested by the visual appearance of the time series with no regard to linearity.

The data processing technique used for intermittency is simply to calculate, for each sensor and for each crossing, the times at which that sensor moved into, or out of, a region containing dye.

4. Results

a. Dye conservation

To understand how dye conservation applies to the experimental data, it is useful to consider (1) in more detail. Let an orthogonal Cartesian coordinate system be oriented so that positive z points vertically upward and the dye dispenser is moving along the y axis at constant speed f, all the while emitting dye at a uniform rate λ over a vertical aperture $z = 0$ to $z = L$. Also, the initial time is chosen so that the dye dispenser crosses the origin of coordinates at time $t = 0$. Then the source function may be written as

$$s(x, y, z, t) = \frac{\lambda}{L}\,\theta(z)\theta(L - z)\delta(x)\delta(y - ft) \qquad (5)$$

where θ is the Heaviside step function. Take (1) and integrate it over the entire x–z plane and over time from negative infinity to time t. Noting that several terms vanish, one obtains

$$Q(y, t) + \frac{\partial}{\partial y}\int_{-\infty}^{t} dt' \int dx'dz'v(x', y, z', t') \times c(x', y, z', t') - \mu\frac{\partial^2}{\partial y^2}\int_{-\infty}^{t} dt' \times \int dx'dz'c(x', y, z', t') = \frac{\lambda}{f}\theta(ft - y) \qquad (6)$$

where

$$Q(y, t) \equiv \int dx'dz'c(x', y, z', t) \qquad (7)$$

and where v is the y-component of the Eulerian velocity field.

The quantity Q is nonnegative and can be estimated for each crossing simply by summing appropriately weighted zero-order moments. The right-hand side of (6) is also nonnegative and can be calculated from known experimental parameters. The second and third terms on the left-hand side of (6) can, of course, not be calculated from the dye data. However, there is no reason for either of them to be preferentially either positive or negative. Hence, it is reasonable to test the validity of the approximate conservation law

$$Q(y, t) \approx \frac{\lambda}{f}\theta(ft - y). \qquad (8)$$

Note that the step function on the right-hand side of (8) is simply a reminder that no dye can be detected in a crossing until the source has gone by.

For the actual measurements, an additional complication was present: two different kinds of dye, rhodamine and fluorescein, were pumped from the dispenser in a mixture. Furthermore, each fluorometer was sensitive to either fluorescein or rhodamine, but not both. There were 15 fluorescein and 10 rhodamine

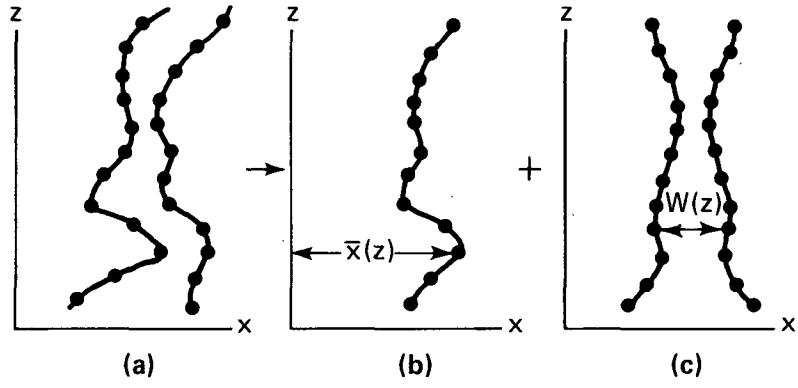

FIG. 6. Decomposition of a dye-sheet cross-section (a) into a centerline (b) specified by the x_{ij} and a symmetrized cross-section (c) specified by the W_{ij}.

fluorometers. Since equal concentrations of each kind of dye were dispensed, it is assumed that each fluorometer underestimated the true concentration by a factor of 2. For the experiment, $\lambda/f = .066$ gm cm^{-1}. In Fig. 7 values of Q, as calculated from the m_{ij0}, are plotted in comparison with λ/f. Imagine that all the fluorometers are numbered serially from top to bottom of the sensor chain. Then the range in Q values shown in Fig. 7 for each crossing is induced by variations which result from including only the even-numbered, only the odd-numbered, or all of the sensors in the calculation of Q. The more adequate the vertical resolution, the more tightly clustered these numbers should be. It is seen that there is reasonable agreement between prediction and experiment, although the induced range in Q is substantial. The reason for the dye shortfall that seems to be present at early and late times is not known.

b. Horizontal advection and shear distortion

We now present results based upon centerlines as defined in Section 3c and illustrated in Fig. 6. It is clear from Figs. 4 and 5 that ambient vertical shear plays a substantial role in the evolution of the dye sheet. If the shear s were perfectly uniform in space and time, all centerlines would be straight lines. Furthermore, if θ is the angle that the centerline makes with the vertical, we would have $\tan\theta = st$, and it would be trivial to measure $\tan\theta$ for each crossing. It is obvious, however, that the shear is highly nonuniform over the vertical aperture spanned by the fluorometers. Therefore, $\tan\theta$ is determined between each adjacent pair of fluorometers and the depth-averaged value of $\tan^2\theta$ calculated, after which the square root is taken. This is done for each crossing. Results for all of the crossings are plotted in Fig. 8. It is seen that a straight line fits these points rather well (correlation coefficient = 0.95). The slope of the least squares linear fit drawn in Fig. 8 is equal to 10.5×10^{-3} sec^{-1}.

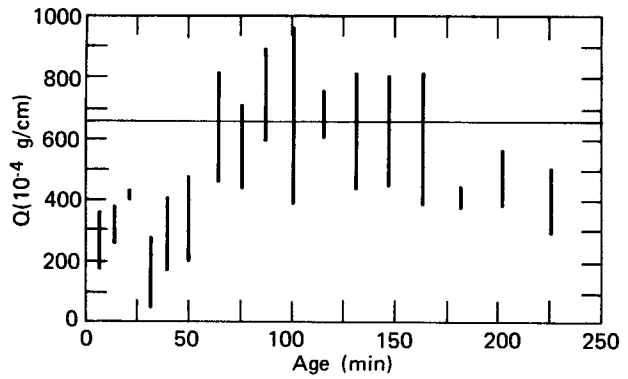

FIG. 7. Dye conservation results. The horizontal line gives the theoretical value.

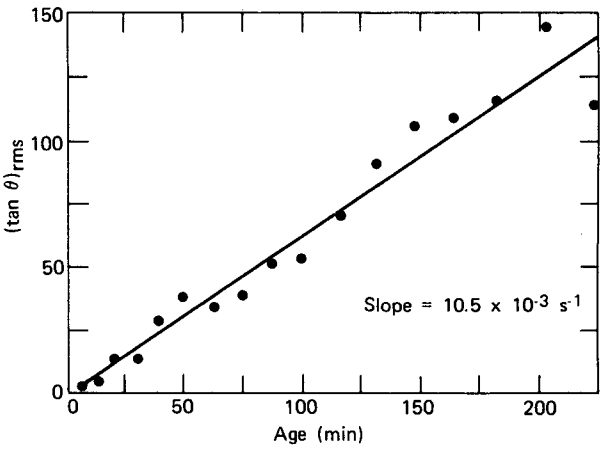

FIG. 8. Values of $(\tan\theta)_{rms}$ versus dye sheet age. The angle θ is chosen so that $(\tan\theta)_{rms} = 0$ would mean that the dye sheet is perfectly vertical.

The foregoing results suggest that, given the linearity already discussed, the centerlines themselves should be markedly similar once horizontal stretching with time is removed. That this may indeed be the case is already apparent from Figs. 4 and 5. To illustrate this point, the horizontal coordinates of each centerline are divided by the corresponding crossing age. This leaves us with an equivalent horizontal current profile for each crossing. These profiles are plotted together in Fig. 9. It is important to note that each of the profiles has been independently translated along the abscissa so that its integral over depth vanishes. This was done because it afforded an objective way to overlay the profiles in the absence of sufficiently accurate navigation data to make absolute comparisons. The range of velocities seen in Fig. 9 is typical for background internal wave horizontal velocity components. The profiles clearly exhibit a strong underlying similarity.

c. Width results

Moving on to second-order moments, we present here results based upon the W_{ij}^2 defined in (4). More specifically, we calculated for each crossing the depth-averaged sum over j of W_{ij}^2. Only fluorometers registering dye are included in the summation. This quantity, which we denote by $\bar{W}^2$, is the depth-averaged width squared of the symmetrized cross section shown in Fig. 6, which illustrates the important point that these are widths that remain after all kinematic shear distortion has been removed. A plot of $\bar{W}^2$ versus crossing age is given in Fig. 10. One sees that a straight line fits the data rather well (correlation coefficient = 0.97) in log–log coordinates. The associated power law dependence is 2.93 ± 0.12.

Since the centerline tends to become nearly horizontal for the later crossings and since the fluorometer

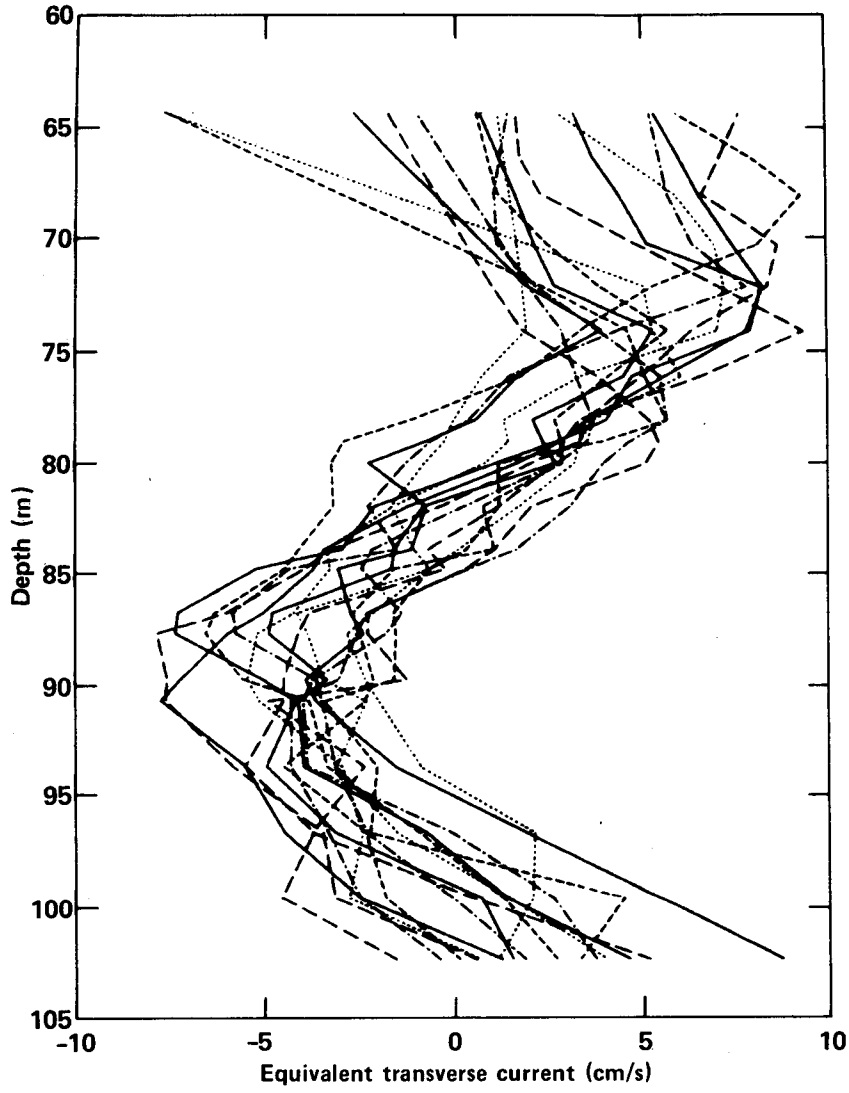

FIG. 9. Equivalent transverse current versus depth for 16 of the dye sheet crossings. This plot is oriented to be compatible with Figs. 4 and 5. Crossing number 4 is not included because insufficient dye was detected to produce a good centerline.

chain does experience depth variations as it is towed, it is necessary to consider the possibility that the width results have been seriously distorted by these variations. We have carried out simulations in which dye sheets with prescribed width-growth power laws have been crossed by fluorometers moving with the highly random depth-variation time series actually experienced during the experiment. It is found that the effect is serious only when the assumed power law is very low, such as $t^{0.25}$. It is also of random size from crossing to crossing, so that, as one would expect from the outset, the correlation coefficient is seriously degraded from the 0.97 found in Fig. 10. In particular, when a width growth more rapid than t^1 is assumed, width distortion is found to be completely negligible.

d. Intermittency

Using the dye transition times described in Section 3d, various elementary measures of intermittency were defined and plotted versus age. The results are shown in Figs. 11–13. It is seen that according to any of these measures, intermittency generally tends to increase or to remain the same with increasing age over the range of experimental values.

5. Theoretical interpretation of width results

It is not difficult to find theoretical arguments and approaches which lead to the observed proportionality of width to the 3/2 power of time. One line of reasoning notes that geophysical spectra are in general

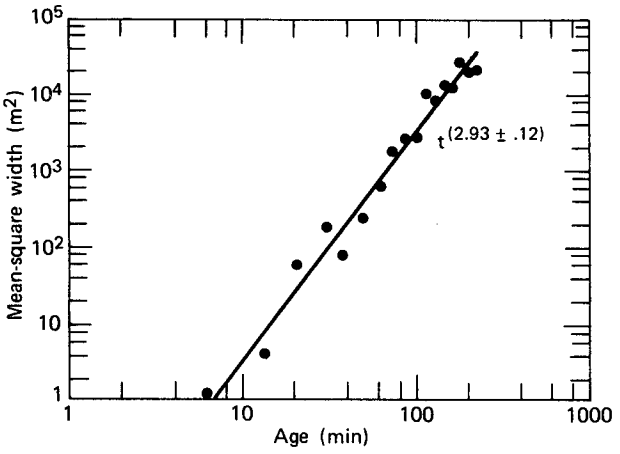

FIG. 10. Mean square width versus age for the 17 dye sheet crossings. The widths are calculated from moments as described in Section 3.

"red," with more variance in the larger scales. Since any two tracer particles are separated most effectively by velocities having a scale of variation on the order of the particles' present separation, it follows that this separation will tend to accelerate as it is acted upon by increasingly energetic velocity scales. This is the content of the empirically derived Richardson's 4/3 law (Richardson, 1926), which states that, for a wide range of scales, the effective diffusivity is proportional to the 4/3 power of the size of the diffusing cloud. This leads directly to a $t^{3/2}$ width dependence. One may obtain the same result by considering a cloud of passive contaminant whose extent lies within the inertial subrange of an isotropic turbulent background. Then dimensional analysis (e.g., Landau and Lifshitz, 1959, p. 123) leads to the square of the width being proportional to ϵt^3, where ϵ is the energy dissipation rate. The experiment discussed here, however, was performed in an environment that was markedly anisotropic.

Another, more detailed, approach focuses upon the interaction of vertical shear and vertical diffusion. The basic mechanism is two-dimensional, and can best be discussed in terms of solutions to the equation

$$\left[\frac{\partial}{\partial t} - \mu \frac{\partial^2}{\partial z^2} + u(z, t) \frac{\partial}{\partial x}\right] c(x, z, t) = s(x, z, t) \quad (9)$$

where μ is now an effective diffusivity which in effect parameterizes the vertical motions. The quantity $u(z, t)$ is the horizontal current as a function of depth and time.

Equation (9) can be solved exactly for a linear profile

$$u(z, t) = sz \quad (10)$$

where the shear s is assumed constant. It is found that, if $W(t)$ is the width of an original point source,

$$W^2(t) = \tfrac{1}{6} \mu s^2 t^3. \quad (11)$$

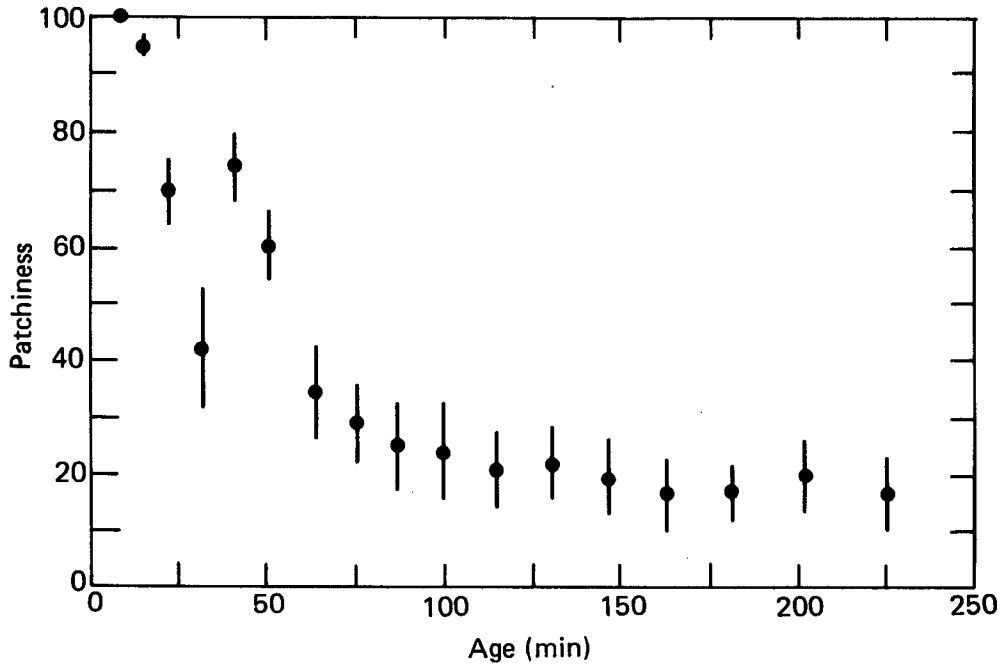

FIG. 11. The average percentage of time that a sensor is actually in dye between first and last detection for each crossing as a function of age.

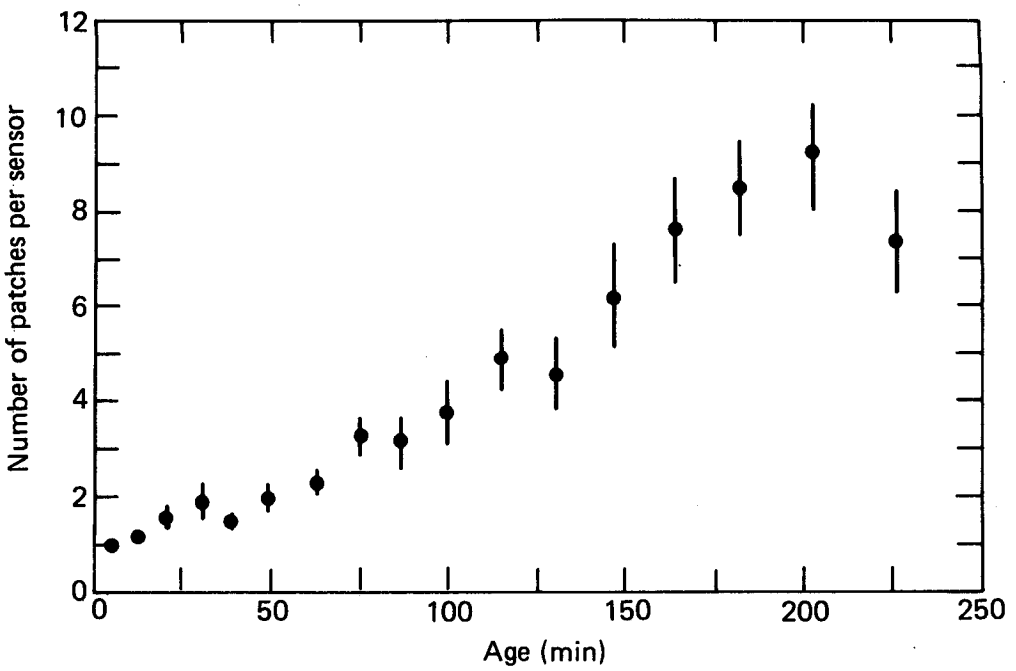

FIG. 12. Mean number of dye patches per sensor for each crossing as a function of age.

Although it has the right form to agree with our results, (11) has the serious difficulty that its derivation depends upon the linearity of the horizontal current profile, a highly dubious proposition in light of Fig. 9. Efforts to explain the widths "locally" in terms of shears at the same depth have not been successful.

On the other hand, (9) does seem to be a reasonable starting point for the problem at hand. It emphasizes

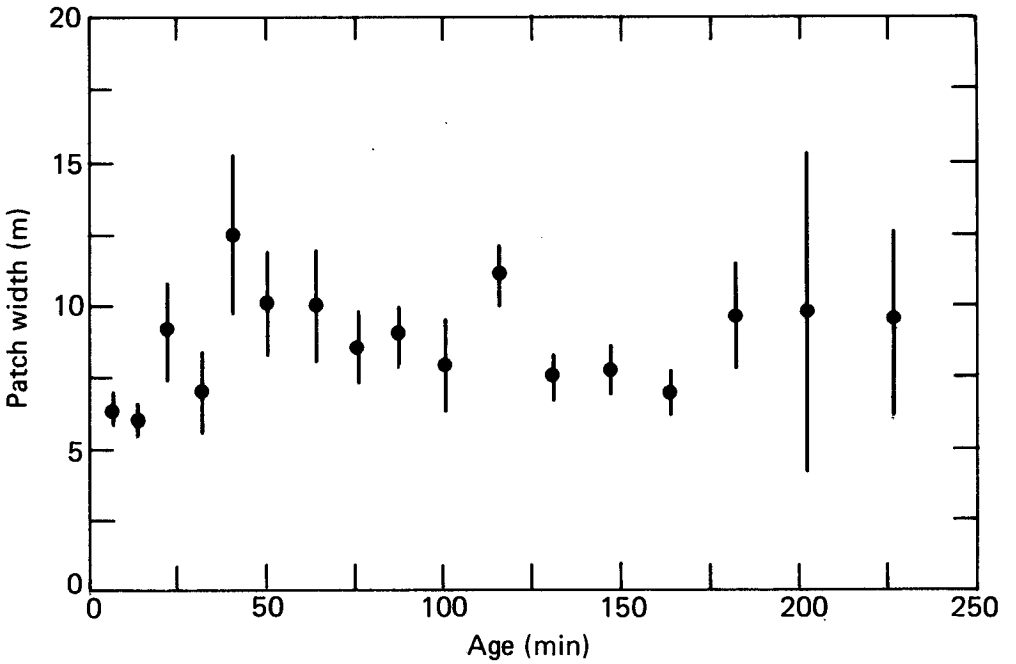

FIG. 13. Mean width of individual dye patches for each crossing versus age.

the role of the horizontal current profile, which is certainly a prominent, rather well-defined feature in the fluorometer data. By subsuming vertical motion into an effective diffusivity, one is hoping to include the important effects of vertical motion while avoiding the substantial additional complexity of having to consider it in detail. One would in general expect, especially in the presence of strong stratification, the vertical component of the velocity field to be much smaller than the horizontal components and to vary over smaller scales in both space and time, properties that tend to justify incorporation into the diffusive part of the equation.

a. General solution

What is clearly required is the ability to extract useful information from (9) for arbitrary $u(z, t)$. This can be done using an approach suggested in recent work by Young *et al.* (1982). Multiply (9) by x^k and integrate over x. Upon integrating the current profile term by parts, one obtains

$$\left(\frac{\partial}{\partial t} - \mu \frac{\partial^2}{\partial z^2}\right) m_k(z, t) = ku(z, t)m_{k-1}(z, t) + s_k(z, t) = r_k(z, t) \quad (12)$$

where

$$m_k(z, t) = \int dx x^k c(x, z, t), \quad (13)$$

$$s_k(z, t) = \int dx x^k s(x, z, t). \quad (14)$$

Equation (12) can be solved recursively to yield m_k for any desired value of k. Using a Green's function approach we have

$$m_k(z, t) = \int dz'dt' g(z - z', t - t')r_k(z', t') \quad (15)$$

$$g(z, t) = \theta(t)\left[\frac{1}{4\pi\mu t}\right]^{1/2} \exp\left(-\frac{z^2}{4\mu t}\right). \quad (16)$$

For a dye-sheet source passing through the x–z plane at $t = 0$, the source function is a product of Dirac delta functions given by

$$s(x, z, t) = c\delta(x)\delta(t) \quad (17)$$

where limitations on the vertical extent of the dye sheet have been ignored. The quantity c is a constant.

It follows quickly from (12)–(17) that

$$m_0(z, t) = c\theta(t) \quad (18)$$

$$m_1(z, t) = c \int dz'dt' g(z - z', t - t')u(z', t')\theta(t') \quad (19)$$

$$m_2(z, t) = 2c \int dz'dt'dz''dt'' g(z - z', t - t') \times u(z', t')g(z' - z'', t' - t'')u(z'', t'')\theta(t''). \quad (20)$$

Write $u(z, t)$ as a Fourier transform in vertical wavenumber k and temporal frequency ω according to

$$u(z, t) = \int dkd\omega a(k, \omega)e^{i(kz-\omega t)}. \quad (21)$$

The current profile is real, so that

$$a(k, \omega) = a^*(-k, -\omega) \quad (22)$$

for all k and ω. Let $W^2(z, t)$ be the width squared of the dye profile at time t and depth z. That is,

$$W^2(z, t) = \frac{m_2(z, t)}{m_0(z, t)} - \left[\frac{m_1(z, t)}{m_0(z, t)}\right]^2. \quad (23)$$

Upon substituting the appropriate expressions into (23) and utilizing (16) along with (21), we find

$$W^2(z, t) = \int dkdqd\omega d\sigma e^{i(k-q)z} \times a(k, \omega)a^*(q, \sigma)B(t; k, q, \omega, \sigma) \quad (24)$$

where

$$\begin{aligned} B(t; k, q, \omega, \sigma) &= e^{-\mu(k-q)^2 t}\left[\frac{e^{i(\sigma-\omega)t+\mu(k-q)^2 t} - 1}{\mu(k - q)^2 + i(\sigma - \omega)}\right] \\ &\times \left(\frac{1}{\mu q^2 + i\sigma} + \frac{1}{\mu k^2 - i\omega}\right) \\ &- e^{-\mu(k-q)^2 t}\left\{\frac{e^{-i\omega t+\mu(k^2-2kq)t} - 1}{[\mu(k^2 - 2kq) - i\omega](\mu q^2 + i\sigma)}\right. \\ &\left. + \frac{e^{i\sigma t+\mu(q^2-2kq)t} - 1}{[\mu(q^2 - 2kq) + i\sigma](\mu k^2 - i\omega)}\right\} \\ &- \left(\frac{e^{-i\omega t} - e^{-\mu k^2 t}}{\mu k^2 - i\omega}\right)\left(\frac{e^{i\sigma t} - e^{-\mu q^2 t}}{\mu q^2 + i\sigma}\right). \end{aligned} \quad (25)$$

b. Early time behavior

When the quantity B is expanded in powers of time, it is found that the constant, linear and quadratic terms all vanish so that

$$B(t; k, q, \omega, \sigma) = \frac{2}{3}\mu kqt^3 + \cdots. \quad (26)$$

Hence, to lowest order in t, W^2 will grow with the observed t^3 dependence. Integrating the leading term in (26) and ignoring higher-order terms, we obtain

$$W^2(z, t) = \frac{2}{3}\mu s^2(z, 0)t^3 \quad (27)$$

where $s(z, 0)$ is the shear at depth z and time $t = 0$. It therefore follows that, for t sufficiently small, the width at each depth is governed by the shear at that depth. If (27) is averaged over depth, we have

$$\overline{W^2(t)} = \frac{2}{3}\mu\overline{s^2}t^3. \quad (28)$$

Insofar as time dependence is concerned, (28) has its confirmation in Fig. 10. If values of $\overline{W^2(t)}t^{-3}$ are calculated for each of the crossings, one obtains the estimate

$$\mu\overline{s^2} = (2.3 \pm 1.1) \times 10^{-4}\ \text{cm}^2\ \text{s}^{-3}. \quad (29)$$

Using the regression in Fig. 8, we have $\overline{s^2} = 1.1 \times 10^{-4}\ \text{s}^{-2}$, or

$$\mu = (2.1 \pm 1.0)\ \text{cm}^2\ \text{s}^{-1}. \quad (30)$$

It is also interesting to analyze fluctuations in $W^2(z, t)$ with depth. From (27) it follows that

$$\overline{V(t)} = \frac{4}{9}\mu^2(\overline{s^4} - \overline{s^2}^2)t^6, \quad (31)$$

where

$$V(t) = \overline{[W^2(z, t) - \overline{W^2(t)}]^2}. \quad (32)$$

The left-hand side of (31) is readily evaluated from the data. These points are plotted in Fig. 14, where the slope of the regression line indicates a $t^{5.78\pm0.23}$ dependence. It is straightforward to calculate $\overline{s^4}$ using the same approach described in Section 4b for $\overline{s^2}$. When this is done, a different estimate for μ arises given by

$$\mu = (2.6 \pm 1.4)\ \text{cm}^2\ \text{s}^{-1}. \quad (33)$$

Hence there is agreement in both the exponent and the coefficient associated with (31).

c. *Implications of universality*

One of the main developments in recent internal wave research (for recent reviews see Olbers, 1983; Levine, 1983) is the emergence of a degree of universality in spectra associated with the deep ocean background (Garrett and Munk, 1972, 1975). In this work, the current components are treated as stationary random processes. Although the data discussed here have been collected in the seasonal thermocline, it is reasonable, and in fact customary, to compare upper ocean results with those implied by the "universal" spectral forms.

To see what these implications are, it is only necessary to treat the Fourier components in (24) as random quantities. In particular, for $u(z, t)$ a stationary random process in space and time one has

$$\langle a(k, \omega)a^*(q, \sigma)\rangle = q^{-2}\delta(k - q)\delta(\omega - \sigma)\Phi(q, \omega) \quad (34)$$

where $\Phi(k, \omega)$ is the shear spectrum. Taking the ensemble average in (34) yields

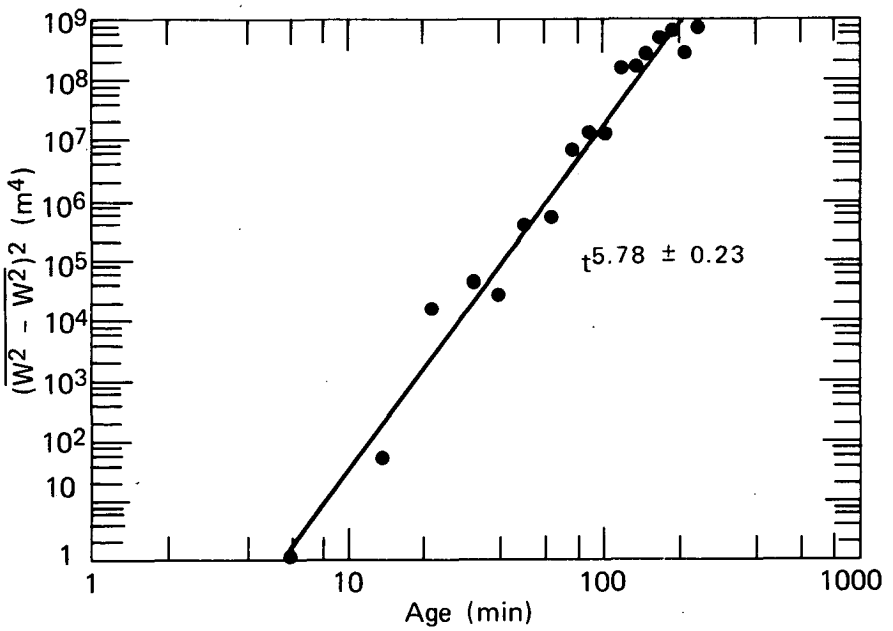

FIG. 14. Variance of $W^2(z, t)$ over depth versus age for the 17 dye sheet crossings. These quantities are defined and calculated as described in Section 5b.

$$\langle W^2(z, t)\rangle = \int dqd\omega F(t; q, \omega)\Phi(q, \omega) \quad (35)$$

where

$$F(t; q, \omega) = q^{-2}(\omega^2 + \mu^2 q^4)^{-2}$$

$$\times [\omega^2 - 3\mu^2 q^4 + \mu q^2 t(\omega^2 + \mu^2 q^4) + 4\mu q^2 e^{-\mu t q^2}$$

$$\times (\mu q^2 \cos\omega t - \omega \sin\omega t) - (\omega^2 + \mu^2 q^4)e^{-2\mu t q^2}]. \quad (36)$$

One new feature that immediately emerges is that, for large t,

$$\langle W^2(z, t)\rangle \approx 2\mu t \int dqd\omega \frac{\Phi(q, \omega)}{\omega^2 + \mu^2 q^4}. \quad (37)$$

For short times, we of course have the usual result, which in the present context can be written as

$$\langle W^2(z, t)\rangle \approx \frac{2}{3}\mu\langle s^2\rangle t^3 \quad (38)$$

where $\langle s^2\rangle$ is the mean-square shear.

Hence the rate of expansion eventually slows from cubic to linear in time. It is intuitively clear that there must be some kind of slowdown, since a perpetually accelerating width would demand the existence of arbitrarily large relative horizontal velocities such as are very difficult to envision if $u(z, t)$ is to be a stationary random process. On the other hand, for a linear velocity profile over an infinite depth range as in (10), perpetual acceleration is clearly possible. The exact manner in which the transition from cubic to linear occurs depends of course upon the details of Φ.

The first of our spectral assumptions is that it factors into a spatial and a temporal part according to

$$\Phi(q, \omega) = S(q)P(\omega). \quad (39)$$

The spatial factor $S(q)$ is set equal to a simplified version of the composite shear spectrum proposed by Gargett *et al.* (1981):

$$S(q) = \langle s^2\rangle[1 + \ln(q_1/q_0)]^{-1}q_0^{-1}, \quad 0 < q < q_0$$

$$= \langle s^2\rangle[1 + \ln(q_1/q_0)]^{-1}q^{-1}, \quad q_0 < q < q_1 \quad (40)$$

where q_0 and q_1 correspond to wavelengths of 10 meters and 1 meter, respectively. Equation (40) is a simplification in the sense that wavenumbers greater than q_1 are ignored. The contributions of high wavenumbers to $\langle W^2\rangle$ are, however, strongly suppressed by the form of F. For the temporal factor we use

$$P(\omega) = \left(\frac{\bar\omega}{\eta}\right)\omega^{-1}(\omega^2 - \bar\omega^2)^{-1/2}, \quad \bar\omega < \omega < N \quad (41)$$

as suggested in the Garrett–Munk models (e.g., Munk, 1981). Here $\bar\omega$ is the inertial frequency, N is the buoyancy frequency, and

$$\eta = \cos^{-1}\frac{\bar\omega}{N}. \quad (42)$$

Incorporating these assumptions for Φ into (35) yields

$$\langle W^2(z, t)\rangle = \frac{\mu\langle s^2\rangle}{\bar\omega^3}[J_1(\bar\omega t) + J_2(\bar\omega t)] \quad (43)$$

where

$$J_1(\tau) = \frac{1}{1 + \ln r}\frac{1}{\eta}\int_0^1 dq \int_0^\eta duG(\tau, \alpha q^2, \sec u), \quad (44)$$

$$J_2(\tau) = \frac{1}{1 + \ln r}\frac{1}{\eta}\int_1^r \frac{dq}{q} \int_0^\eta duG(\tau, \alpha q^2, \sec u), \quad (45)$$

$$\alpha = \frac{\mu q_0^2}{\bar\omega}, \quad r = q_1/q_0 = 10 \quad (46)$$

$$G(\tau, x, y) = x^{-1}(x^2 + y^2)^{-2}[y^2 - 3x^2 + 2x\tau(x^2 + y^2)$$

$$+ 4x\tau(x\cos y\tau - y\sin y\tau)e^{-x\tau} - (x^2 + y^2)e^{-2x\tau}]. \quad (47)$$

The quantities J_1 and J_2 are readily calculated numerically using a Monte Carlo technique. In Fig. 15, $\langle W^2(t)\rangle$ is plotted versus $\bar\omega t$ for a variety of vertical diffusivities. Also included are the experimental points shown in Fig. 10. The value of $\mu\langle s^2\rangle$ indicated in (29) is used throughout. This insures that the levels of the three curves and that of a t^3 line drawn through the data will coincide as t approaches zero. The range of diffusivities represented by the curves corresponds to the range within which most other measurements of this quantity also fall (Garrett, 1979).

It is interesting to note that the data in Fig. 15 tend to favor values of μ that are below the range indicated in (30). If we regard $\mu\overline{s^2}$ as fixed at the value indicated in (29), we are led to the possibility that simply squaring the slope in Fig. 8 leads to an underestimate of $\overline{s^2}$. This is plausible because of the finite spacing of the fluorometers, which produces the effect of a low-pass filter. In particular, one has

$$\langle[u(z + \Delta z, t) - u(z, t)]^2\rangle(\Delta z)^{-2}$$

$$= 2(\Delta z)^{-2}\int dqd\omega q^{-2}(1 - \cos q\Delta z)\Phi(q, \omega) \quad (48)$$

where Δz is the vertical separation between adjacent fluorometers. The left-hand side of (48) can be calculated from the data. Note that, as $\Delta z \to 0$, the right-hand side of (48) approaches $\langle s^2\rangle$. In practice, $\Delta z = 1$, 2, or 3 meters. From (39)–(41) we have

$$\langle[u(z + \Delta z, t) - u(z, t)]^2\rangle(\Delta z)^{-2} = \frac{2\langle s^2\rangle}{q_0(1 + \ln r)(\Delta z)^2}$$

$$\times\left[\int_0^{q_0}\frac{dq}{q^2}(1 - \cos q\Delta z) + q_0\int_{q_0}^{q_1}\frac{dq}{q^3}(1 - \cos q\Delta z)\right]. \quad (49)$$

The left-hand side is now calculated over all available

data for each of the three separations. For Δz = 1, 2, and 3 meters, (49) becomes respectively

$$163.2 = 0.72\ \langle s^2 \rangle$$
$$90.7 = 0.52\ \langle s^2 \rangle$$
$$78.5 = 0.40\ \langle s^2 \rangle \qquad (50)$$

in units of 10^{-6} s^{-2}. This leads directly to an estimate of mean-square shear of

$$\langle s^2 \rangle = (200 \pm 25) \times 10^{-6}\ \text{s}^{-2}. \qquad (51)$$

Hence the estimate of mean-square shear increases by almost a factor of 2 when (40) is postulated for the spectrum. (It is assumed here that ensemble averages can be equated with vertical averages.) That the values of $\langle s^2 \rangle$ implied in (50) are more closely spaced than the left-hand sides of these relations lends credence to the spectral assumption. If (29) and (51) are used we have, instead of (30),

$$\mu = (1.0 \pm 0.5)\ \text{cm}^2\ \text{s}^{-1}. \qquad (52)$$

6. Raster plot geometry and shear

A basic question that immediately arises in the interpretation of towed fluorometer chain data is how much information these data really contain, since they are only two-dimensional slices of a three-dimensional world. So far, it has been freely assumed that no problems arise from ignoring the existence of the spatial dimension along which the dye source travels. This is particularly true in (8) and (9). Of course, in these cases the agreement of theory and experiment furnishes some evidence that this is a good approximation. In the present section, however, we examine an important question in which the validity of the approximation can be examined more quantitatively. In particular, to what extent can the shear estimate at some depth, as calculated from a Raster plot (such as Fig. 4), and a knowledge of crossing age be equated to the oceanic shear component transverse to the path of the dye source?

The striking similarities in shapes and magnitudes of the equivalent current profiles shown in Fig. 9 almost directly suggest a lowest-order kinematic model for the dye centerlines. The model can most easily be derived by assuming that all molecular diffusion and vertical dye motion can be ignored and that the horizontal current **u** is a function of z alone. Under these assumptions, the dye signals for any crossing form a pattern congruent with the centerline. Consider a small piece of dye that is emitted at some particular depth z by a source moving with a horizontal velocity **v**. This source may be viewed as a vertical line that continuously emits dye over a continuous range of depths as it is towed with velocity **v**. Upon emission, the piece of dye is transported by an ambient current **u**(z), which is assumed to have only horizontal components. Let t_0 be any convenient initial time and let

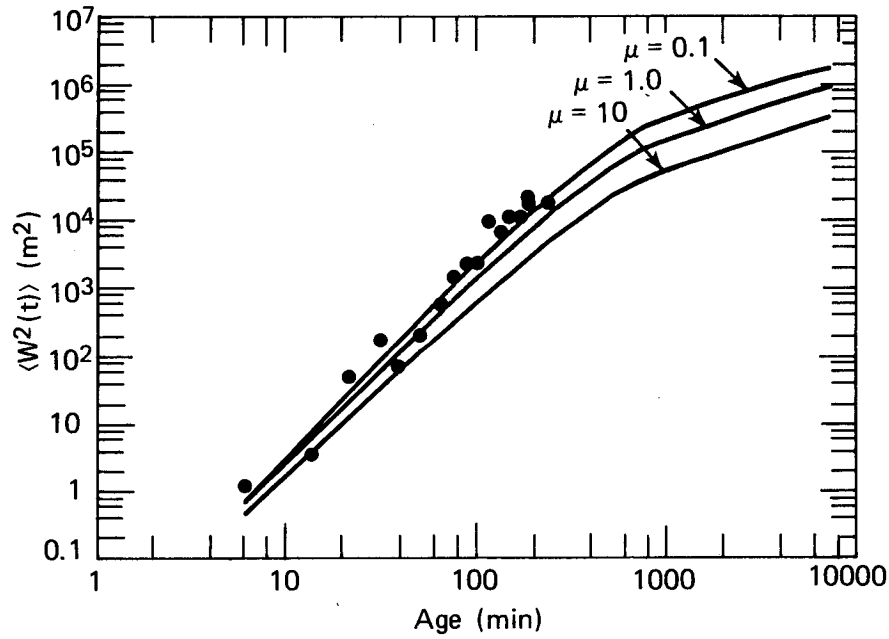

FIG. 15. Plots of $\langle W^2(z, t) \rangle$ versus t as given in (43) for different values of the vertical diffusivity μ. The units of μ are cm^2 s^{-1}. All three curves are for $\mu\ \langle s^2 \rangle = 2.3 \times 10^{-4}$ cm^2 s^{-3}, as given in (29). Also shown are the experimental points.

$\mathbf{r}_0$ be the corresponding source position vector. Then the source position at any time t is given by

$$\mathbf{r} = \mathbf{r}_0 + \mathbf{v}(t - t_0). \tag{53}$$

Suppose the piece of dye has been in the water a length of time τ before it is detected at position $\mathbf{r}$ and time t. For this to happen, one must have

$$\mathbf{r} - \mathbf{r}_0 - \mathbf{v}(t - t_0) = \tau[\mathbf{u}(z) - \mathbf{v}]. \tag{54}$$

Equation (54) defines the dye sheet geometry model. The interpretation is made that each fluorometer passes through the center of mass of its signal at a space–time point ($\mathbf{r}$, t) that satisfies this relation.

Suppose now that the moving surface described by (54) is "cut" by a vertical line of dye sensors moving with crossing velocity $\mathbf{f}$. Let the inverse slope (at some depth z) of the centerline as recorded on the Raster plot be denoted by dx/dz. Let the age of the crossing (as defined in Section 2) be denoted by a. Then, after a bit of algebra, one obtains

$$\frac{1}{a}\frac{dx}{dz} = \lambda \frac{s_\perp + \lambda s_{||}(u_\perp/v)}{\sin\alpha - \lambda(u_\perp/f)(1 - f_{||}/v)} \tag{55}$$

where $s_\perp$ and $s_{||}$ are respectively shear components transverse and parallel to the source direction. Also, α is the crossing angle such that $\cos\alpha = \hat{f}\cdot\hat{v}$, and

$$\lambda = (1 - u_{||}/v)^{-1}. \tag{56}$$

It is seen from (55) that, by conducting the experiment in such a way that $\sin\alpha \approx 1$, $f_{||} \ll v$, and $v, f \gg u$, all need to be concerned with axial components disappears and the two-dimensional approximation is a good one. These conditions were met for the experiment described in this work.

7. General comments and conclusions

The results presented in previous sections suggest an interrelated pattern of effects that can be more or less arranged in order of increasing "sophistication." The most obvious such effect is the strong kinematic advection that acts in the horizontal. Our findings are consistent with the horizontal currents associated with a random internal wave background being the primary mechanism for the observed centerline distortion. The high correlations observed from crossing to crossing are consistent with these currents being dominated by an inertial time scale, and also imply that the horizontal correlation extends to many kilometers. In these particular respects, the upper ocean data considered here agree with the Garrett–Munk model of background internal waves.

Although vertical motions are much smaller by comparison and were not directly observed in this experiment, they must play an essential role. Without them, there would be no way for the observed width growth to occur. The success of (28) is good evidence that this width growth is in fact the combined effect of vertical diffusion and shear. The value of vertical diffusivity in (52) is consistent with what has been described in a recent review (Garrett, 1979) as the "traditional" value, although it is substantially larger than values derived from microstructure. As the review points out, however, the general subject of vertical diffusivities in the ocean is a complicated one which is by no means closed. Another point of consistency is that with μ in the ranges implied by (33) or (52), the dye did not have enough time to diffuse vertically to any significant extent beyond the fluorometer aperture, in agreement with the observed absence of a progressive decrease in the amount of dye detected from crossing to crossing. The question of how long the t^3 growth is sustained can only be answered when something is known about the $a(q, \omega)$. If "universality" in the form of (39)–(41) is assumed, we find from Fig. 15 that $\langle W^2(z, t)\rangle$ is nearly cubic to sufficiently large times for consistency with the data. A final point of agreement is that both theory and experiment indicate a power-law dependence which is a bit less than cubic in time. In this regard, it would be of particular interest to conduct an experiment out to perhaps an order of magnitude greater maximum dye sheet age in order to observe the transition from cubic to linear behavior.

The "highest order" effect considered here, at least in the sense of being the most difficult to understand quantitatively, is that of intermittency. The basic problem is that on one hand intermittency consists of apparent discontinuities in the dye concentration field as sampled by horizontally moving fluorometers, whereas on the other hand there is no reason to believe that a solution to (9) with a source term given by (17) has any possibility whatever of developing discontinuities in the horizontal at finite times. In other words, the observed intermittency is a more detailed effect than can be understood on the basis of (9). When the object is to explain intermittency, it is evidently an oversimplification to parameterize the vertical motions with an effective diffusivity. It would appear that the only way to attack the problem is actually, either numerically or theoretically, to track individual particles in an appropriately chosen Eulerian velocity field.

A key experimental decision which greatly facilitated the analysis was the selection of the dye sheet geometry. This configuration leads to the very simple boundary condition (17), which is perhaps the best possible from the viewpoint of confronting (9) with experimental data. The results of Section 6 further support the choice of experimental parameters, implying in the process that theoretical analyses that exclude the longitudinal dimension merit consideration.

Acknowledgments. Many people contributed to the success of the experiment. They include Carl J. Gundersdorf and Charles W. Anderson (TFC systems engineers), Gary S. Keys (fluorometer engineer), John W. Giles, Jr. (dye system scientist), and Theodore R. Whyte and Howard H. Wright (dye system engineers). We also thank Professor O. M. Phillips for helpful comments and suggestions regarding the analysis.

REFERENCES

Ewart, T. E., and W. P. Bendiner, 1981: An observation of the horizontal and vertical diffusion of a passive tracer in the deep ocean. *J. Geophys. Res.*, **86**, 10 974–10 982.

Gargett, A. E., P. J. Hendricks, T. B. Sanford, T. R. Osborn and A. J. Williams, III, 1981: A composite spectrum of vertical shear in the upper ocean. *J. Phys. Oceanogr.*, **11**, 1258–1271.

Garrett, C. J. R., 1979: Mixing in the ocean interior. *Dyn. Atmos. Oceans*, **3**, 239–265.

——, and W. H. Munk, 1972: Space-time scales of internal waves. *Geophys. Fluid Dyn.*, **2**, 225–264.

——, and ——, 1975: Space-time scales of internal waves: A progress report. *J. Geophys. Res.*, **80**, 291–297.

Keys, G. S., and B. F. Hocheimer, 1977: The design of a simple fluorometer for underwater detection of rhodamine dye. *Sea Technol.*, **18**, 24–29.

Kullenberg, G., 1977: Observations of the mixing in the Baltic thermo- and halocline layer. *Tellus*, **29**, 572–587.

Landau, L. D., and E. M. Lifshitz, 1959: *Fluid Mechanics*. Pergamon, 536 pp.

Levine, M. D., 1983: Internal waves in the ocean: A review. *Rev. Geophys. Space Phys.*, **21**(5), 1206–1216.

Munk, W. H., 1981: Internal waves and small scale processes. *Evolution of Physical Oceanography*, B. A. Warren and C. Wunsch, Eds., MIT Press, 264–291.

Olbers, D. J., 1983: Models of the oceanic internal wave field. *Rev. Geophys. Space Phys.*, **21**(7), 1567–1606.

Richardson, L. F., 1926: Atmospheric diffusion shown on a distance-neighbour graph. *Proc. Roy. Soc. London*, **A110**, 709–737.

Young, W. R., P. B. Rhines and C. J. R. Garrett, 1982: Shear flow dispersion, internal waves and horizontal mixing in the ocean. *J. Phys. Oceanogr.*, **12**, 515–527.